

## ARTICLE OPEN



# Localized corrosion induced surface modifications of Al-Cu-Li alloy studied by ToF-SIMS 3D imaging

Meicheng Li<sup>1</sup>, Antoine Seyeux<sup>1</sup>, Frédéric Wiame<sup>1</sup>, Philippe Marcus<sup>1</sup> and Jolanta Światowska<sup>1</sup>✉

Three-dimensional (3D) time-of-flight secondary ion mass spectrometry (ToF-SIMS) imaging is a promising tool in the analysis of surface modifications of alloy matrix and intermetallic particles induced by localized corrosion due to its good spatial resolution and very high sensitivity to chemical identification especially involving light mass elements like Li. In this paper, ToF-SIMS 3D chemical mapping combined with scanning electron microscopy was performed to study the localized corrosion of Al-Cu-Li alloy (AA2050-T8) in a region around an Al-Cu-Fe-Mn intermetallic particles (IMPs) in 0.1 M NaCl solution. Initiation of corrosion was locally observed on the IMPs and between IMPs and matrix substrate. Moreover, a modified oxide/hydroxide layer was observed over IMPs compared to the matrix. This new corrosion layer was enriched with chlorides and Cu hydroxides. ToF-SIMS 3D imaging revealed that Li was present over the alloy matrix, while no Li was present over the IMPs in regions where localized corrosion occurred.

*npj Materials Degradation* (2021)5:23; <https://doi.org/10.1038/s41529-021-00170-9>

## INTRODUCTION

Localized corrosion of Al alloys is known to be the most frequent cause of failure of high-strength aluminium alloys<sup>1,2</sup>. The less common intergranular or transgranular corrosion can also be considered a precursor of stress corrosion cracking (SCC) or a potential origin for fatigue cracks<sup>3–6</sup>. The corrosion is not only a lateral surface modification and breakdown of surface oxide but also can lead to in-depth modifications of the oxide and underlying alloy matrix. The localized corrosion is generally related to the chemical heterogeneities in the alloy such as intermetallic particles (IMPs). It has been shown that the Al-Cu-Fe-Mn-rich IMPs are the preferential sites of localized corrosion initiation in Al alloys due to the galvanic effect<sup>3–6</sup>. However, it is widely known that cathodic IMPs can become anodic during exposure to corrosive media<sup>7</sup>. Birbilis et al.<sup>8</sup> revealed that the initially cathodic Al-Cu-Fe IMPs in AA7075 lead to the localized corrosion between matrix and IMPs, a phenomenon termed as trenching. This peripheral corrosion is also often referred to as ‘cathodic corrosion’<sup>9,10</sup>. In further stages, intergranular corrosion attack and/or exfoliation can develop<sup>11</sup>. However, here a discussion on more advanced stages of corrosion is beyond the scope of this paper. Boag et al.<sup>12</sup> have also shown that preferential corrosion sites of the AA2024 Al-Cu-Mg alloy in NaCl electrolyte are associated with the presence of Al-Cu-Fe-Mn particles. This IMP-induced localized corrosion has been usually investigated by conventional techniques such as scanning electron microscopy (SEM) and energy-dispersive X-ray spectroscopy (EDX)<sup>13,14</sup>. Some local techniques such as atomic force microscopy (AFM)<sup>15</sup>, scanning Auger spectroscopy<sup>16</sup>, and scanning Kelvin probe force microscopy (SKPFM)<sup>17,18</sup>, and especially in situ techniques such as in situ SKPFM<sup>7</sup> have focused more precisely on local morphological or chemical surface modifications to reveal the influence of IMPs on the corrosion behavior of Al alloys.

Based on the current state of the art, several 3D imaging techniques can be highlighted such as scanning transmission electron microscopy (STEM), X-ray computed tomography, etc.<sup>19–22</sup>. In electron microscopy tomography (EMT), a series of EMT images from the same sample can be collected through a wide range of

angles and depth from which a 3D image can be reconstructed. The corrosion behavior of cast aluminium alloy A356 and 316 L stainless steel<sup>23–26</sup>, was studied by means of EMT and X-ray CT, respectively, to reveal the 3D spatial structure of corrosion site. These works demonstrated morphological and structural modifications induced by corrosion and pretreatment such as de-alloying of S phase (Al<sub>2</sub>CuMg) particles in an AA 2024-T3 aluminium alloy with the preferential dissolution of Mg and Al leading to the formation of a sponge-like structure with a nanosize porosity with Cu enrichment<sup>23</sup>. A more advanced analysis method is the synchrotron X-ray tomography, which is a well-established and non-destructive technique with the relatively high resolution in the range of micrometer<sup>27,28</sup>.

ToF-SIMS three-dimensional (3D) imaging, applied here in this study, is a surface sensitive technique allowing chemical analysis of low amounts (typically in the range of ppm down to ppb) of light mass elements. It can be applied for the analysis of all types of solids. It is a unique method allowing to obtain explicit information of the surface and in-depth chemical structure and elemental distribution in order to better understand the corrosion mechanisms of heterogeneous materials. A dual-beam mode allows for the spatial detection and in-depth distributions of elements in 3D space<sup>29</sup>. This technique has been used in various applications, such as biological, medical and chemical<sup>30–35</sup>. Concerning the corrosion behavior and surface treatments, 3D ToF-SIMS imaging was used to study the localized corrosion behavior of Mg (99%)<sup>36</sup> and Mg alloy<sup>37</sup>, respectively. It showed the influence of ultra-low amounts of metallic impurities that were non-homogeneously distributed (Fe, Mn, Al) at the grain boundaries (GBs) on different corrosion-active GBs.

Different chemical structures of the passive film<sup>38</sup> or trivalent conversion coatings over IMP and Al matrix of AA2024 were revealed by ToF-SIMS 3D imaging<sup>39</sup>. The local surface heterogeneities, such as various IMPs in the Al alloy matrix<sup>40,41</sup>, have paramount importance in forming an oxide layer with different composition. They can invoke surface reactivities and lead to localized corrosion. The objective of the presented work is to understand the localized corrosion mechanisms that take place at

<sup>1</sup>Chimie ParisTech - CNRS, PSL University, Institut de Recherche de Chimie Paris, 11 rue Pierre et Marie Curie, Paris 75005, France. ✉email: [jolanta.swiatowska@chimieparistech.psl.eu](mailto:jolanta.swiatowska@chimieparistech.psl.eu)

heterogeneous surfaces, which are responsible for the local surface breakdown. Thus, ToF-SIMS is an appropriate surface sensitive technique, which can be applied to perform a systematic set of measurement on different types of heterogeneities. Moreover, due to the high detection limits of light elements, this technique is also widely applied for the analysis of Li in the Li-containing alloys<sup>42,43</sup>, or Li in electrode materials used in Li-ion batteries<sup>44,45</sup>. Therefore, based on the high sensitivity to low-atomic-mass element such as Li and the applicability of spatial detection, ToF-SIMS chemical imaging is considered as a promising technique for the study of Al-Cu-Li alloys.

In this paper, ToF-SIMS 3D imaging was combined with SEM/EDX characterization to study the surface modifications of AA2050-T8 (Al-Cu-Li) alloy during the first stages of corrosion. This paper aims to demonstrate the advantages of the surface sensitive technique such as ToF-SIMS in localized corrosion studies of heterogeneous materials in order to obtain new information and/or to confirm some existing hypothesis on corrosion mechanisms.

## RESULTS AND DISCUSSION

### Microstructure and ToF-SIMS 2D chemical imaging before corrosion

The SEM images in Fig. 1(a, b) and (c, d) show the Al-Cu-Fe-Mn IMPs in the 'a region of interest' (ROI) before and after the corrosion experiment. The EDX analysis performed in the bottom part of the IMPs (as indicated in Fig. 1(b) by a red rectangle) shows that the chemical composition was 72 at% Al, 13 at% Cu, 8 at% Fe and 8 at% Mn. However, the chemical composition of the IMPs is heterogeneous because of the visible contrast similar to those observed previously<sup>46,47</sup>. The EDX analysis of different

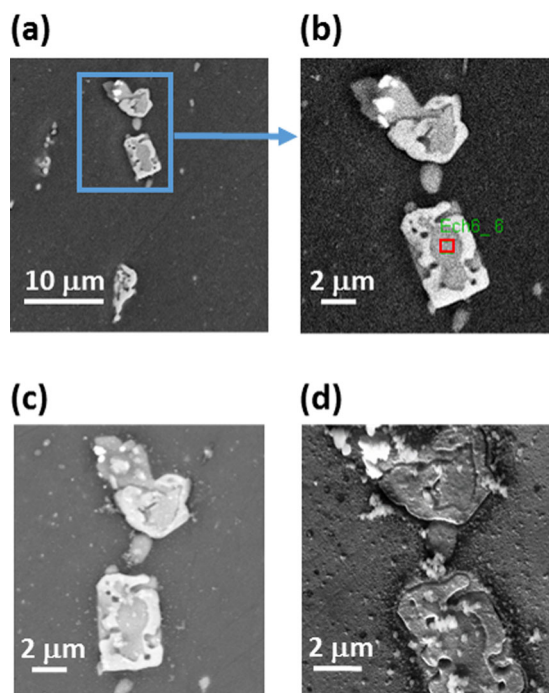


**Fig. 1 SEM images of AA2050-T8 sample with the ROI containing Al-Fe-Cu-Mn IMPs.** Samples before immersion: (a) SE image showing the ROI with lower magnification, (b) BSE image with the highlighted region (red rectangle) showing the EDX analysis area; Samples after immersion in 0.1 M NaCl (c) SE image and (d) BSE image showing the ROI after corrosion exposure. The image (a) corresponds to the 2D and 3D ToF-SIMS images presented hereafter; the images b–c are the magnified area of the blue rectangle zone shown in fig. (a).

particles (not presented here) showed the enrichment of Cu and Fe for the brighter particles or brighter parts of particles. The quantity of Cu and Fe were assessed to be  $17 \pm 2$  at% and  $7 \pm 1$  at%, respectively.

Next, the same sample region presented in Fig. 1 (a) was analyzed by ToF-SIMS 2D chemical mapping using a positive mode to sense metal elements<sup>36,38</sup>. Before analysis, the native surface oxide layer was removed by a slight sputtering. The ToF-SIMS 2D data shows a high intensity of  $\text{Cu}^+$ ,  $\text{Fe}^+$ , and  $\text{Mn}^+$  signals and lower signals of  $\text{Al}^+$  in the area of IMP being in-line with the EDX results indicating that the particles contain Al-Cu-Fe-Mn phase. The advantage of ToF-SIMS over the EDX is the possibility to detect the low weight elements such as Li. Lower intensity of Li signal observed in ToF-SIMS 2D mapping (Fig. 2,  $\text{Li}^+$ ) in Al-Fe-Cu-Mn IMPs compared to the alloy matrix, indicates that Li is dissolved in the matrix. This can be confirmed by our previous TEM results<sup>48</sup>, and other bibliographic data<sup>49</sup>, showing that Li in AA2050-T8 is principally observed in the T1 phase ( $\text{Al}_2\text{CuLi}$ ), which is homogeneously distributed in the matrix. However, other studies by Electron energy-loss spectroscopy<sup>50</sup> and soft X-ray emission spectroscopy<sup>51</sup> showed that Li can be observed in the Al-Fe-Cu-Mn.

### Microstructural characterization after corrosion

After immersion of AA2050-T8 sample in 0.1 M NaCl electrolyte for 45 min initiation of corrosion over the Al-Cu-Fe-Mn IMPs and a trenching around the IMPs can be observed as shown in secondary electron (SE) image in Fig. 1(d). The backscattered electron (BSE) image (in Fig. 1 (c)) does not show clear modifications with reference to the pristine sample (Fig. 1(a) and (b)). The corrosion of aluminium alloys occurs by an enhanced dissolution of Al and/or lightweight elements from the Al alloy matrix close to the Al-Cu-Fe-Mn IMPs, which is induced by the galvanic coupling between the cathodic IMPs and more anodic alloy matrix<sup>52,53</sup>, especially during the first stages of corrosion. However, it should be noted that the compositional heterogeneity within the IMP mentioned above, (Fig. 1a) can result also in initiation of localized corrosion attack inside the IMP as observed by SEM in Fig. 1b and as reported previously<sup>46,54</sup>

### ToF-SIMS 3D chemical imaging after corrosion

Figure 3 shows the ToF-SIMS 3D chemical images of the ROI after the corrosion experiment. Figure 3(a) (b) and (c) show the 3D maps of  $\text{AlO}_2\text{H}^-$  ( $m = 59.9812$  u),  $\text{AlO}_2^-$  ( $m = 58.9728$  u) and  $\text{Al}_2^-$  ( $m = 53.9634$  u) signals. These signals are characteristic of Al oxide<sup>36,38,40,41</sup>, Al hydroxide and Al metal, respectively.  $\text{AlO}_2^-$  and  $\text{AlO}_2\text{H}^-$  show a homogeneous and high intensity of Al oxide/hydroxide signal over the whole analyzed volume. The lower intensity of  $\text{AlO}_2^-$  signal over the IMPs presented in the plane view of the 3D image may be due to the morphology effect of corroded surface and/or the oxide breakdown over this area. In Fig. 3(c), the increased intensity of  $\text{Al}_2^-$  in the bottom of the cube of aluminium alloy matrix region (at the oxide/metal interface after 300 s of sputtering) is seen but not over the IMPs region. The difference of  $\text{Al}_2^-$  intensity means that within the sputtering depths (300 s), the oxide/IMP interface was not reached, but the oxide/matrix interface was reached. It should also be noticed that the lower  $\text{Al}_2^-$  signal intensity over the IMPs after sputtering may have been influenced by the preferential dissolution of Al (onset of corrosion) and/or a lower quantity of Al in the IMPs than in the alloy matrix. The differences in the intensity of  $\text{Al}_2^-$  in the area of IMPs and matrix will be discussed hereafter.

The data for  $\text{Cl}^-$  ( $m = 34.9696$  u) and  $\text{OH}^-$  ( $m = 17.0048$  u) are shown in Fig. 3(d) and (e), respectively, indicating corrosion products and some residues of NaCl.  $\text{Cl}^-$  is present all over the outermost surface (Fig. 3(d)).  $\text{Cl}^-$  signals became then confined into a narrow space at lower sites but within the oxide layer. The

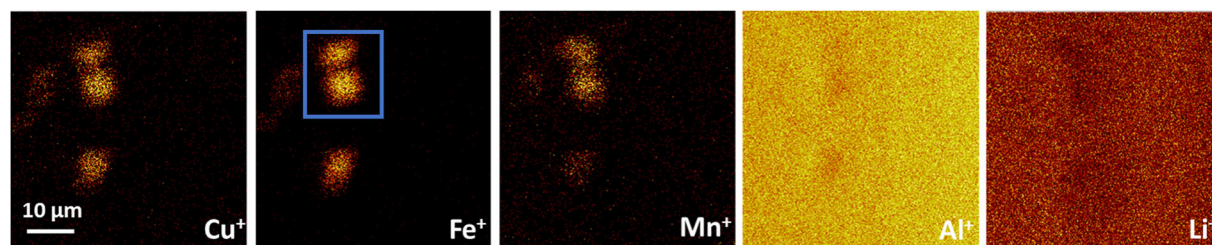


**Fig. 2** ToF-SIMS 2D chemical images of the pristine AA2050-T8 sample. Images of  $50\ \mu\text{m} \times 50\ \mu\text{m}$  performed in positive mode ( $\text{Cu}^+$ ,  $\text{Fe}^+$ ,  $\text{Mn}^+$ ,  $\text{Al}^+$ ,  $\text{Li}^+$  ions) in the ROI comprising selected Al-Fe-Cu-Mn IMPs. A blue rectangle marked in the  $\text{Cu}^+$  image corresponds to the region of SEM micrograph presented in Fig. 1 (b-d).

latter was seen only locally over the IMPs. The local chloride enrichment over the IMPs inside the oxide layer is furthermore seen from the overlapping of the  $\text{Cl}^-$  (green in Fig. 3(d)) and  $\text{Cu}^-$  signals (orange in Fig. 3(f)), where the  $\text{Cu}^-$  signal corresponds to the Cu-rich IMPs. This higher intensity of  $\text{Cl}^-$  over the IMPs is clearly observed in the plane view map of  $\text{Cl}^-$ . Moreover, a slightly higher intensity of  $\text{OH}^-$  (Fig. 3(e)) is also observed in the bulk of the oxide in the IMPs region. Differently to the distribution of  $\text{Cl}^-$ , some  $\text{OH}^-$  signal is also observed in the matrix region. The presence of  $\text{OH}^-$  in the matrix over the whole depth of the oxide corroborates with the high intensity of  $\text{AlO}_2\text{H}^-$ . The presence of chlorides and hydroxides over the corroded area confirms the localized corrosion as usually reported in the literature<sup>16,38,55</sup>. However here, we demonstrate a local distribution of the Cl and OH in the bulk of the oxide layer, over the zones corresponding to the Cu-rich IMPs.

$\text{Cu}^-$  ( $m = 62.9268\ \text{u}$ ),  $\text{CuOH}^-$  ( $m = 79.9354\ \text{u}$ ) and  $\text{Li}^-$  ( $m = 7.0168\ \text{u}$ ) signals are also shown (in Fig. 3(f), (g) and (h), respectively) to represent the distribution of the principle alloying elements.  $\text{Cu}^-$  and  $\text{CuOH}^-$  ion signals (Fig. 3(f) and (g), respectively) show higher intensities over IMP region through the oxide layer, similar to the  $\text{Cl}^-$  and  $\text{OH}^-$  signals. The enrichment in more noble elements such as Cu on the surface of corroded areas was reported previously<sup>9,56–59</sup>. The origin of this enrichment can be the preferential dissolution of Al induced by local submicron sized compositional heterogeneities within the IMP. Here, our results show that  $\text{CuOH}^-$  signal in the matrix region is lower than in the IMP region (plane view image in Fig. 3(g)). The spatial distribution of  $\text{OH}^-$  is similar to  $\text{CuOH}^-$ , indicating that copper hydroxide is one of the corrosion products. Moreover, within the oxide layer (cube view images), the higher intensities of  $\text{OH}^-$  and  $\text{CuOH}^-$  signals over the IMPs regions can be confirmed. In the case of  $\text{Cu}^-$  (cube view image in Fig. 3(f)), a more intense signal is observed not only over the IMPs region within the oxide but also at the oxide/metal interface. The Cu enrichment at this interface indicates the presence of metallic copper in the alloy substrate.

Fig. 3(h) shows a homogenous distribution of Li through the oxide layer in the 3D image of  $\text{Li}^-$  signal ( $m = 7.0168\ \text{u}$ ). However, the plane view clearly shows that almost no or a very low Li signal is observed over the IMPs, indicating a local Li dissolution. These results agree with our previous findings where no Li was observed in the area of corrosion<sup>38</sup>. However, the lower signal intensity over the IMP can also be a result of sputtering time not sufficient to reach the oxide /metal interface over this region or preferential dissolution of Al and other light elements like Li in the corrosion zone comprising the IMPs.

In order to compare the distribution of the most characteristic species on the surface and inside the oxide, the  $\text{AlO}_2^-$ ,  $\text{Cl}^-$  and  $\text{Cu}^-$  ions were overlaid as shown in Fig. 4. For clarity, the image treatment was processed to adjust the relative intensity signals using Ion-Spec software. As discussed above (Fig. 3 b), the  $\text{AlO}_2^-$  is observed in the whole analyzed volume. A significant difference in

chemical composition can be observed between IMP and matrix region. The  $\text{Cl}^-$  signal shows a high intensity over the first seconds of sputtering corresponding to the top surface of the alloy and then the increased intensity is measured above Cu-rich IMP as observed previously for  $\text{Al}_2\text{Cu}$  IMPs in Al-Cu model alloy<sup>40</sup>. At the oxide/alloy substrate interface Cu enrichment is also evidenced over the matrix region.

### ToF-SIMS ion depth profiles after corrosion

To gain more insights into the differences between IMPs region and matrix after corrosion, the ion depth profiles were reconstructed from 3D images. As shown schematically in Fig. 5 (a), three regions can be distinguished on the AA2050 alloy after corrosion: the green matrix region (A) ~78% of the total surface, the blue IMP region (B) ~2% and the rest, gray area (C), considered as the boundary between IMPs and matrix. The ion depth profiles corresponding to matrix (green, (A)) and IMPs (blue, (B)) were plotted separately to see in details the surface and bulk composition. The gray region (C) was excluded as a transitory region between the matrix and the IMPs. In order to be able to compare the intensity of different ions for IMP (Fig. 5 (b)) and matrix (Fig. 5 (c)) regions, the signal intensity was normalized.

The signal intensity variations as a function of sputtering time reflect the modifications of the chemical composition and the structure of the analyzed oxide as a function of depth.  $\text{OH}^-$ ,  $\text{AlO}_2\text{H}^-$  and  $\text{AlO}_2^-$  ion depth profiles for both matrix (Fig. 5 (b)) and IMPs (Fig. 5(c)) have similar intensity and shape, possibly indicating a similar chemical structure of the aluminium oxide/hydroxide layer over both regions. However, the low  $\text{Al}_2^-$  signal intensity in the area of IMPs (in Fig. 5 (c)) over the whole sputtering time (300 s), indicates a lower metallic aluminium signal intensity over the IMPs region than the matrix, which means that the oxide/metal substrate interface has not been reached after 300 s sputtering. In the case of the matrix region (Fig. 5(b)), a step intensity increase of  $\text{Al}_2^-$  signal from  $10^2$  to  $10^4$  observed from 200 s of sputtering indicates that the interface with substrate region was almost attained. The longer sputtering time necessary to reach the oxide/metal interface for the IMPs can be related to the formation of corrosion layer with a different composition over the IMPs than the layer over the matrix region, like demonstrated in our previous work<sup>38</sup>. Due to immersion in NaCl electrolyte, the large difference in corrosion potentials of more noble Cu-rich IMP and less noble Al-based matrix as well as local micrometric chemical heterogeneities within the IMPs (as shown in Fig. 1) leads to microgalvanic coupling. As a consequence, the dissolution of the Al alloy in the vicinity of IMP and also the preferential dissolution of Al inside the IMPs occur leaving Cu remnant above IMPs. The Al dissolution conducts to the particle dealloying<sup>52</sup>. The possible initially thinner oxide layer over the Cu-rich IMPs compared to Al matrix, as demonstrated in our previous studies<sup>40</sup>, leads to an enhanced local cathodic reactivity over the IMP and a high rate of oxygen reduction reaction, as shown by DFT calculations<sup>60</sup>. This implies the corrosion initiation in the Cu-rich

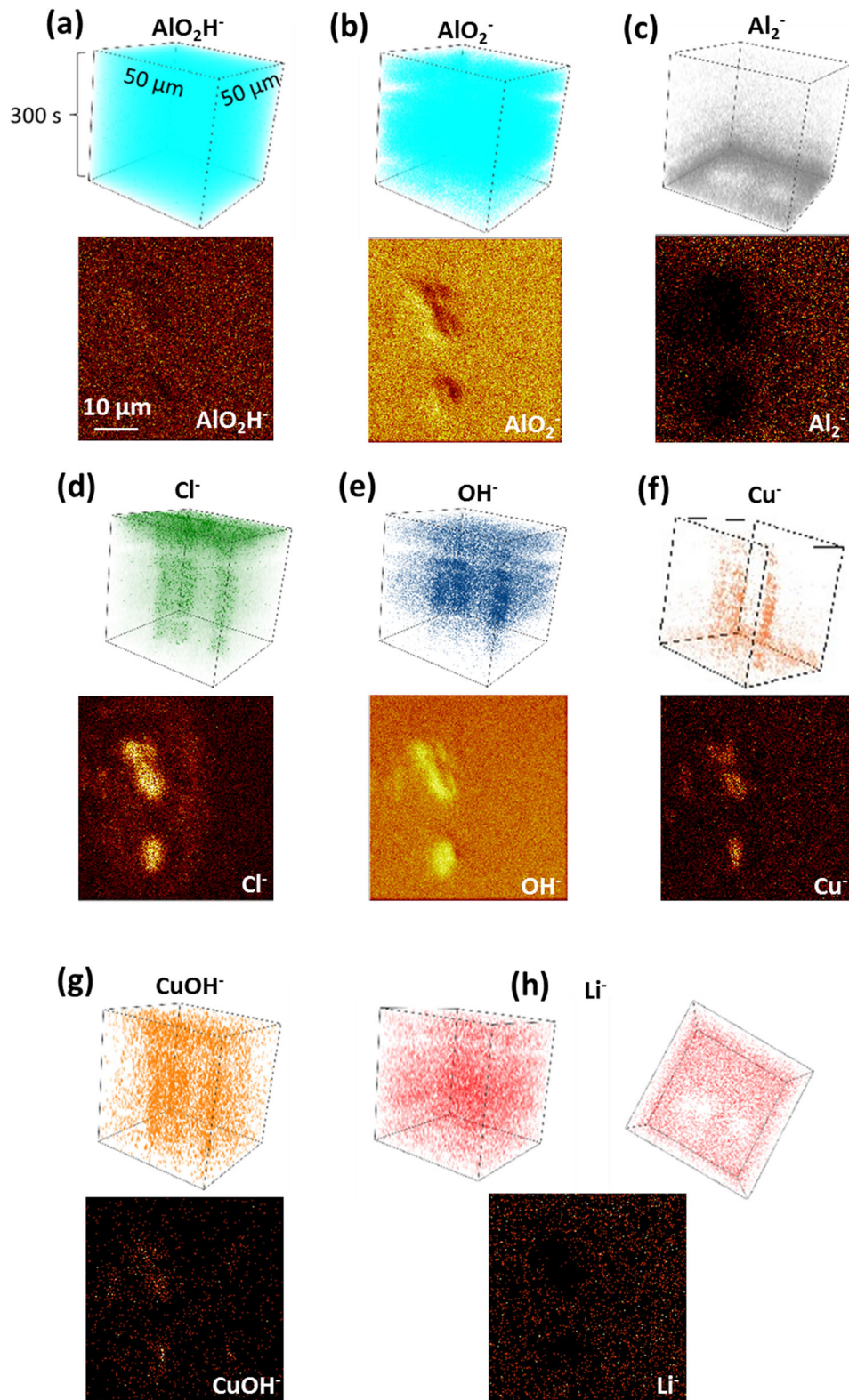


**Fig. 3 ToF-SIMS 3D chemical images of AA2050-T8 sample after corrosion.** 3D images ( $50\ \mu\text{m} \times 50\ \mu\text{m} \times 300\ \text{s}$ ) and corresponding plane views (by stacking 2D slices at different depths) obtained after immersion of AA2050-T8 sample in 0.1 M NaCl (**(a)**  $\text{AlO}_2\text{H}^-$ , **(b)**  $\text{AlO}_2^-$ , **(c)**  $\text{Al}_2^-$ , **(d)**  $\text{Cl}^-$ , **(e)**  $\text{OH}^-$ , **(f)**  $\text{Cu}^-$ , **(g)**  $\text{CuOH}^-$ , **(h)**  $\text{Li}^-$  (additional 3D top view image) in the ROI comprising a selected Al-Fe-Cu-Mn IMP.

IMPs and then the corrosion propagation with dissolution of Al matrix leading to the trenching as observed by time depended SKPFM studies on Al-Cu-Fe-Mn particles in AA7075-T6<sup>52</sup>. In the further stages, both continuous cathodic and anodic reactions will

enhance locally the formation of a new layer enriched with the corrosion products (chlorides and copper hydroxides as confirmed by  $\text{Cl}^-$ ,  $\text{Cu}^-$  and  $\text{CuOH}^-$  signals) over IMP and/or near IMP (Fig. 5 (b) and (c)). The enrichment of the  $\text{Cl}^-$  through entire oxide layer

above IMPs (Fig. 5(c)) while a rapid decrease of the  $\text{Cl}^-$  signal in the Al matrix from the top of surface to the interface is observed (Fig. 5(b)). The high intensity of  $\text{Cu}^-$  and  $\text{CuOH}^-$  signals is seen on IMPs (Fig. 6(c)). However, in the case of ion depth profiles obtained for the Al matrix region (Fig. 5(b)), a very low signal of  $\text{CuOH}^-$  and the corresponding  $\text{Cu}^-$  signal keeps increasing from oxide to the interface. The low intensity of  $\text{CuOH}^-$  indicates negligible corrosion to have occurred on the matrix. The increased intensity of  $\text{Cu}^-$  at the oxide/substrate interface shows the presence of metallic Cu in the substrate.

A significant difference between the depth profile of Li in the IMPs and in the matrix is observed. Li is detected in the oxide layer on the matrix (Fig. 5 (b)) while no trace of Li was found over the IMP region (Fig. 5(c)). The presence of Li in the oxide over the matrix can be explained by a high stability of the oxide and almost no corrosion occurring in this area, which agrees with our previous results on corrosion of AA 2050 using 2D ToF-SIMS chemical mapping<sup>38</sup>. The lack of Li signal in the corrosion layer formed over the IMPs can indicate a dissolution of Li as discussed above (Fig. 3

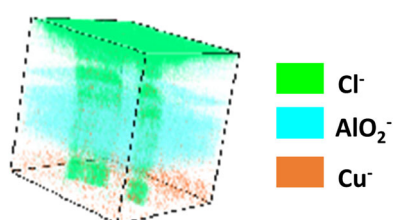


**Fig. 4 ToF-SIMS 3D chemical map with overlaid signals.** 3D image ( $50\ \mu\text{m} \times 50\ \mu\text{m} \times 300\ \text{s}$ ) after corrosion of AA2050-T8 sample in 0.1 M NaCl showing the overlaid signals of  $\text{AlO}_2^-$  (blue),  $\text{Cl}^-$  (green) and  $\text{Cu}^-$  (orange) obtained in the ROI. Individual maps for the  $\text{AlO}_2^-$ ,  $\text{Cl}^-$  and  $\text{Cu}^-$  signals are presented in Fig. 3 (b), (d) and (f), respectively.

(h)). However, it should be noted that lower Li signal intensity over the IMPs than over the matrix on the polished AA 2050 sample (Fig. 2) was already observed. The positive and negative ion intensities, performed on the pristine sample and corroded samples, respectively, cannot be directly compared.

Using the in-depth ion profiles, the oxide and/or corrosion layer thicknesses can be also discussed. As discussed above, the intensity differences for  $\text{Cl}^-$  and  $\text{Cu}^-$ ,  $\text{CuOH}^-$  and  $\text{Li}^-$  ion depth profiles over the IMPs and matrix indicate some variations in the composition of layers formed in the two regions. However, the principal compounds of the oxide ( $\text{AlO}_2^-$ ,  $\text{O}_2^-$ ) and hydroxide

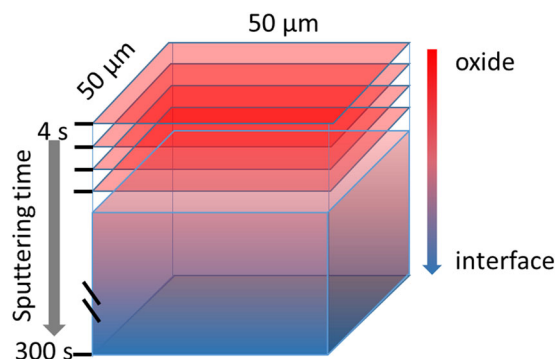


**Fig. 6 Schematic illustration of the principle of 3D ToF-SIMS map reconstruction.** Successive 2D chemical images (with a size of  $50\ \mu\text{m} \times 50\ \mu\text{m}$ ) were acquired at a sputtering time of 4 s per frame (in a total of 76 images) beginning from the outermost surface progressing down to the alloy interface (corresponding to 300 s of incremental sputtering toward the depth). These 2D images are overlaid to generate a three-dimensional (3D) visualization of the sputtered volume. The analysis was performed in the ROI comprising the IMPs and the matrix.

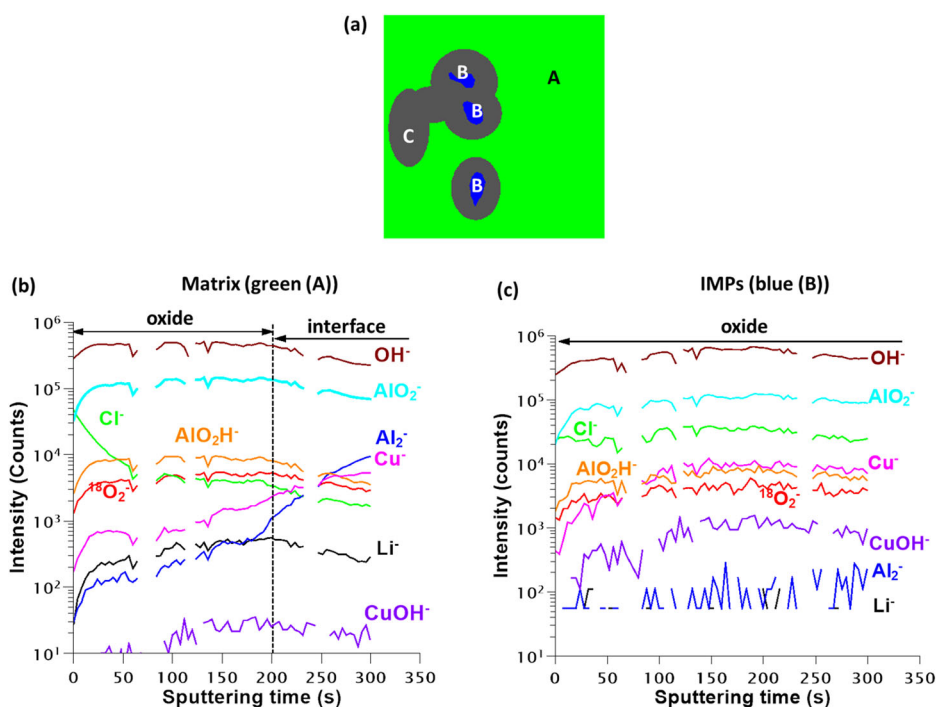


**Fig. 5 Localized in-depth ToF-SIMS profiling.** (a) Reconstructed ToF-SIMS 3D image of the ROI presented in Figs. 2–4 showing three regions corresponding to matrix (green (A)), IMPs (blue (B)) and boundary between IMPs and matrix (gray (C)); (b) ToF-SIMS ion depth profiles of matrix region corresponding to the green area (A); (c) ToF-SIMS ion depth profiles of IMPs region corresponding to the blue area (B). The signal intensity was normalized by the analyzed area.

**Table 1.** Specifications (wt%) of alloying elements in AA2050-T8 alloy.

Element	Cu	Li	Mg	Zn	Mn	Ag	Zr(max)	Fe(max)	Si (max)
wt%	3.2–3.9	0.7–1.3	0.2–0.6	0–0.25	0.2–0.5	0.2–0.7	0.14	0.1	0.08

(OH<sup>-</sup>) show similar intensities (Fig. 5), thus a small intensity increase of Cl<sup>-</sup> and Cu<sup>-</sup>, CuOH<sup>-</sup> and Li<sup>-</sup> signals cannot significantly influence the sputtering rates of layers over IMP and matrix. Since the sputtering time of the oxide above IMP is at least 1.5 times longer than that of the matrix, it suggests a higher oxide thickness over the IMPs. The formation of thicker oxides over the IMPs for the corroded Al alloy was demonstrated previously<sup>38</sup>. Davoodi et al.<sup>17</sup> used AFM/SECM to study the topography of corroded Al alloy and a greater height was observed on the IMPs (AlMnFe), but this protrusion of the IMP was explained by their slower dissolution kinetics of the oxide layer over IMPs and the attack of IMPs. However, due to the limitation their analysis techniques, it was difficult to identify if the local protrusion was induced by the thicker oxide and/or the difference in the topography of metal substrate. With other techniques such as TEM or FIB-SEM, it is also difficult to detect the fragile and not stable oxide layer after corrosion. Cu enrichment and the enhanced oxide coverage was observed along the attacked Al-Cu-Fe-Mn particle/matrix interface region by SKPFM and AFM studies of AA7075-T6 corrosion<sup>52</sup>. Similarly, to the former studies, it can be concluded that here our results confirm that Al-Cu-Fe-Mn IMPs, with the higher quantity of noble elements (most particularly Cu), are prone to initiate localized corrosion. It is followed by surface modifications with formation of corrosion layer with a slightly different composition than the layer over the matrix. Based on the results, the higher layer thickness over the IMPs can be also proposed, however to firmly confirm this hypothesis further analyses are necessary. The dissolution of surrounding matrix can occur in further stages of corrosion.

The combined different modes of ToF-SIMS characterization (3D imaging and ion depth profiling) allowed to have more insights into the mechanisms of corrosion initiation of AA2050-T8 alloy and to evidence structure and chemical composition of the layer over the IMPs and the alloy matrix. A high sensitivity and high detection limit of ToF-SIMS allowed us to visualize a distribution of low atomic mass species like Li. Negligibly low amounts of Li was observed in the oxide over the IMPs while Li was detected in the oxide over the matrix. The layer over the IMPs was thicker than over the Al matrix and enriched in Cl, OH and Cu.

Finally, it should be noted ToF-SIMS 3D chemical imaging can be considered as a one of the most appropriate techniques to perform more systematic measurements on various IMPs and compared to alloy matrices in order to better understand the influence of substrate heterogeneity on the surface reactivity and the initiation and propagation of localized corrosion. However, the studies on corrosion propagation can be limited by this surface sensitive technique when significant morphological modifications and increased surface roughness are observed.

## METHODS

### Samples

AA2050-T8 (Al-Cu-Li) alloy plate (with a thickness of 3 mm) provided by Constellium, France, was cut to specimens of 8.0 mm × 8.5 mm. The specification of the alloy is presented in Table 1. The samples were ground with SiC papers down to 4000-grit size (EU grades), followed by polishing using alumina suspensions down to 0.3 μm particle size to achieve mirror-surface finishing. Then, the samples were successively sonicated in isopropanol, ethanol and finally Ultrapure (UP) Millipore water, and then dried by a stream of filtered compressed air. Then, the samples were

immersed at room temperature (~25 °C) in 0.1 M NaCl electrolyte of around 75 ml (VWR, 99.9% & UP Millipore® water, resistivity >18 MΩ cm) for 45 min. Then, the specimens were taken out from the solution and rinsed with UP Millipore® water, dried and transferred to the respective instrument for ToF-SIMS and/or SEM analysis.

### Surface characterization

The local surface and in-depth chemical modifications are discussed including low-atomic-mass species. To do so, the same sample region named 'a region of interest' (ROI) including an Al-Cu-Fe-Mn IMP, nearby particles and surrounding matrix was selected and characterized before and after immersion in 0.1 M NaCl.

The ToF-SIMS measurements were performed with the IONTOF ToFSIMS<sup>5</sup> spectrometer (IONTOF GmbH, Münster, Germany) operated under high vacuum (10<sup>-9</sup> mbar). A ROI containing Al-Cu-Fe-Mn IMPs was selected. A fiducial marker was deposited on the surface using Cs<sup>+</sup> ions of the Ion-ToF spectrometer for cross-correlative image tracking. The ROI was first (before immersion test) characterized by SEM and EDX (Fig. 1 a–b). Then, the sample including ROI was chemically analyzed this time by 2D ToF-SIMS chemical imaging (in this mode almost no surface degradation is induced). The specimen was then subjected to corrosion by immersing it in 0.1 M NaCl solution at room temperature for 45 min. After the immersion test, chemical 3D ToF-SIMS analysis was performed using a dual-beam mode with pulsed Bi<sup>+</sup> and Cs<sup>+</sup> beams (primary ion beam and sputtering beam, respectively) under burst alignment image mode. The latter resulted in chemical mapping with a spatial resolution of ~200 nm. The initially wide primary Bi beam was split into four small pulses (Burst mode) to achieve a mass resolution of the order of M/ΔM ~6000 (measured on the Si peak).

The polished surface of the specimen was slightly sputtered by a 45° 2 keV Cs<sup>+</sup> beam of 100 nA current to remove the native oxide layer in order to perform 2D imaging of the metallic substrate that was biased with positive polarity using a 25 keV pulsed primary Bi<sup>+</sup> beam of 0.1 pA. The conditions of removal of the native oxide were optimized by repeated depth profiling on the same sample but in different regions. Then, for the corroded specimen, 3D imaging was performed in negative polarity using the same Cs<sup>+</sup> sputtering beam and a 25 keV primary Bi<sup>+</sup> beam delivering 0.3 pA. A schematic presentation of the principle of 3D ToF-SIMS chemical mapping based on 2D successive maps recorded after sputtered layers from the sample surface to the oxide/metal interface over the sputtering depth of 300 s is shown in Fig. 6. The sputtering time between each 2D chemical mapping was 4 s. The final reconstructed 3D chemical mapping represents a stack of 2D maps performed at different depths. For both measurements (2D and 3D), the sputtered area was 1000 μm × 1000 μm and the analyzed area was 50 μm × 50 μm. Treatment of ToF-SIMS data, lateral shift correction on reconstructed 3D images were automatically done on the Cl<sup>-</sup> images, using the Ion-Spec software (version 6.8). The 3D ToF-SIMS chemical maps were stacked to each other and shown in 3D view (cube) (see Figs. 3 and 4).

### Microstructure characterization

SEM and EDX measurement were performed using the Zeiss Ultra55 SEM to define an ROI comprising Al-Fe-Cu-Mn IMPs and the surrounding matrix and study the morphological modifications induced by corrosion in 0.1 M NaCl electrolyte. EDX measurements were performed with the EDX Bruker system using 15 kV as an accelerating voltage.

### DATA AVAILABILITY

The data that support the findings of this study are available from the corresponding author upon reasonable request.

Received: 25 November 2020; Accepted: 7 April 2021;  
Published online: 18 May 2021

## REFERENCES

- Szklarska-Śmiałowska, Z. Pitting corrosion of aluminum. *Corros. Sci.* **41**, 1743–1767 (1999).
- Rao, K. S. & Rao, K. P. Pitting corrosion of heat-treatable aluminium alloys and welds: a review. *Trans. Indian Inst. Met.* **57**, 593–610 (2004).
- Elboujdaini, M. & Revie, R. Metallurgical factors in stress corrosion cracking (scc) and hydrogen-induced cracking (HIC). *J. Solid State Electrochem.* **13**, 1091–1099 (2009).
- Tsai, W.-T. & Chen, M.-S. Stress corrosion cracking behavior of 2205 duplex stainless steel in concentrated nacl solution. *Corros. Sci.* **42**, 545–559 (2000).
- Chen, G., Wan, K.-C., Gao, M., Wei, R. & Flournoy, T. Transition from pitting to fatigue crack growth—modeling of corrosion fatigue crack nucleation in a 2024-T3 aluminum alloy. *Mater. Sci. Eng.: A* **219**, 126–132 (1996).
- Sankaran, K., Perez, R. & Jata, K. Effects of pitting corrosion on the fatigue behavior of aluminum alloy 7075-T6: modeling and experimental studies. *Mater. Sci. Eng.: A* **297**, 223–229 (2001).
- Liew, Y. H. et al. In-Situ Time-Lapse SKPFM Investigation of Sensitized AA5083 Aluminum Alloy to Understand Localized Corrosion. *J. Electrochem. Soc.* **167**, 141502 (2020).
- Birbilis, N., Cavanaugh, M. & Buchheit, R. Electrochemical behavior and localized corrosion associated with Al<sub>7</sub>Cu<sub>2</sub>Fe particles in aluminum alloy 7075-T651. *Corros. Sci.* **48**, 4202–4215 (2006).
- Leclère, T. J. & Newman, R. C. Self-regulation of the cathodic reaction kinetics during corrosion of AlCu alloys. *J. Electrochem. Soc.* **149**, B52–B56 (2002).
- Laurent, C., Scenini, F., Monetta, T., Bellucci, F. & Curioniet, M. The contribution of hydrogen evolution processes during corrosion of aluminium and aluminium alloys investigated by potentiodynamic polarisation coupled with real-time hydrogen measurement. *npj Mater. Degrad.* **1**, 6 (2017).
- Zhang, W. & Frankel, G. S. Transitions between pitting and intergranular corrosion in AA2024. *Electrochim. Acta* **48**, 1193–1210 (2003).
- Boag, A., Hughes, A., Glenn, A., Muster, T. & McCulloch, D. Corrosion of AA2024-T3 Part I: Localised corrosion of isolated IM particles. *Corros. Sci.* **53**, 17–26 (2011).
- Trdan, U. & Grum, J. SEM/EDS characterization of laser shock peening effect on localized corrosion of Al alloy in a near natural chloride environment. *Corros. Sci.* **82**, 328–338 (2014).
- Chemin, A. et al. Influence of Al<sub>7</sub>Cu<sub>2</sub>Fe intermetallic particles on the localized corrosion of high strength aluminum alloys. *Mater. Des.* **53**, 118–123 (2014).
- Davoodi, A., Pan, J., Leygraf, C. & Norgren, S. Integrated AFM and SECM for in situ studies of localized corrosion of Al alloys. *Electrochim. Acta* **52**, 7697–7705 (2007).
- Grilli, R., Baker, M. A., Castle, J. E., Dunn, B. & Watts, J. F. Localized corrosion of a 2219 aluminium alloy exposed to a 3.5% NaCl solution. *Corros. Sci.* **52**, 2855–2866 (2010).
- Davoodi, A., Pan, J., Leygraf, C. & Norgren, S. The role of intermetallic particles in localized corrosion of an aluminum alloy studied by SKPFM and integrated AFM/SECM. *J. Electrochem. Soc.* **155**, C211–C218 (2008).
- Örnek, C., Leygraf, C. & Pan, J. Real-Time Corrosion Monitoring of Aluminum Alloy Using Scanning Kelvin Probe Force Microscopy. *J. Electrochem. Soc.* **167**, 081502 (2020).
- Lidke, D. S. & Lidke, K. A. Advances in high-resolution imaging—techniques for three-dimensional imaging of cellular structures. *J. Cell Sci.* **125**, 2571–2580 (2012).
- Bushby, A. J. et al. Imaging three-dimensional tissue architectures by focused ion beam scanning electron microscopy. *Nat. Protoc.* **6**, 845 (2011).
- Egan, C. et al. 3D chemical imaging in the laboratory by hyperspectral X-ray computed tomography. *Sci. Rep.* **5**, 15979 (2015).
- Hanna, R. D. & Ketcham, R. A. X-ray computed tomography of planetary materials: a primer and review of recent studies. *Geochem* **77**, 547–572 (2017).
- Hashimoto, T. et al. Investigation of dealloying of  $\delta$  phase (Al<sub>2</sub>CuMg) in AA2024-T3 aluminium alloy using high resolution 2D and 3D electron imaging. *Corros. Sci.* **103**, 157–164 (2016).
- Mingo, B., Arrabal, R., Pardo, A., Matykina, E. & Skeldon, P. 3D study of intermetallics and their effect on the corrosion morphology of rheocast aluminium alloy. *Mater. Charact.* **112**, 122–128 (2016).
- Laleh, M. et al. Two and three-dimensional characterisation of localised corrosion affected by lack-of-fusion pores in 316L stainless steel produced by selective laser melting. *Corros. Sci.* **165**, 108394 (2020).
- Chen, B. et al. Three-dimensional structure analysis and percolation properties of a barrier marine coating. *Sci. Rep.* **3**, 1177 (2013).
- Bleuet, P. et al. 3D chemical imaging based on a third-generation synchrotron source, TrAC Trends in Analytical Chemistry. *Corros. Sci.* **29**, 518–527 (2010).
- Vallabhaneni, R., Stannard, T. J., Kaira, C. S. & Chawla, N. 3D X-ray microtomography and mechanical characterization of corrosion-induced damage in 7075 aluminium (Al) alloys. *Corros. Sci.* **139**, 97–113 (2018).
- Jung, S., Foston, M., Kalluri, U. C., Tuskan, G. A. & Ragauskas, A. J. 3D chemical image using ToF-SIMS revealing the biopolymer component spatial and lateral distributions in biomass. *Angew. Chem. Int. Ed.* **51**, 12005–12008 (2012).
- Fletcher, J. S. Latest applications of 3D ToF-SIMS bio-imaging. *Biointerphases* **10**, 018902 (2015).
- Zheng, L., Wucher, A. & Winograd, N. Chemically alternating Langmuir-Blodgett thin films as a model for molecular depth profiling by mass spectrometry. *J. Am. Soc. Mass Spectrom.* **19**, 96–102 (2011).
- Vaidyanathan, S. et al. Subsurface biomolecular imaging of streptomyces coelicolor using secondary ion mass spectrometry. *Anal. Chem.* **80**, 1942–1951 (2008).
- Fletcher, J. S., Rabbani, S., Henderson, A., Lockyer, N. P. & Vickerman, J. C. Three-dimensional mass spectral imaging of HeLa-M cells—sample preparation, data interpretation and visualization. *Rapid Commun. Mass Sp.* **25**, 925–932 (2011).
- Robinson, M. A., Graham, D. J. & Castner, D. G. ToF-SIMS depth profiling of cells: zcorrection, 3D imaging, and sputter rate of individual NIH/3T3 fibroblasts. *Anal. Chem.* **84**, 4880–4885 (2012).
- Niehuis, E. et al. In-situ ToF-SIMS and SFM measurements providing true 3D chemical characterization of inorganic and organic nanostructures. *Microsc. Microanal.* **20**, 2086–2087 (2014).
- Mercier, D., Swiatowska, J., Zanna, S., Seyeux, A. & Marcus, P. Role of segregated iron at grain boundaries on Mg corrosion. *J. Electrochem. Soc.* **165**, C42–C49 (2018).
- Esmaily, M., Malmberg, P., Shahabi-Navid, M., Svensson, J. & Johansson, L. A ToF-SIMS investigation of the corrosion behavior of Mg alloy AM50 in atmospheric environments. *Appl. Surf. Sci.* **360**, 98–106 (2016).
- Li, M., Seyeux, A., Wiame, F., Marcus, P. & Światowska, J. Insights on the Al-Cu-Fe-Mn intermetallic particles induced pitting corrosion of Al-Cu-Li alloy. *Corros. Sci.* **176**, 109040 (2020).
- Stoica, A.-I. et al. Influence of post-treatment time of trivalent chromium protection coating on aluminium alloy 2024-T3 on improved corrosion resistance. *Surf. Coat. Technol.* **369**, 186–197 (2019).
- Cornette, P., Zanna, S., Seyeux, A., Costa, D. & Marcus, P. The native oxide film on a model aluminium-copper alloy studied by XPS and ToF-SIMS. *Corros. Sci.* **174**, 108837 (2020).
- Seyeux, A. et al. ToF-SIMS imaging study of the early stages of corrosion in Al-Cu thin films. *J. Electrochem. Soc.* **158**, C165 (2011).
- Sodhi, R. N. Time-of-flight secondary ion mass spectrometry (ToF-SIMS):—versatility in chemical and imaging surface analysis. *Analyst* **129**, 483–487 (2004).
- Heard, D. W. et al. Interfacial morphology development and solute trapping behavior during rapid solidification of an Al–Li–Cu alloy. *Acta Mater.* **61**, 1571–1580 (2013).
- Li, J.-T. et al. XPS and ToF-SIMS study of Sn–Co alloy thin films as anode for lithium ion battery. *J. Power Sources* **195**, 8251–8257 (2010).
- Golodnitsky, D. et al. Progress in three-dimensional (3D) Li-ion microbatteries. *Solid State Ion.* **177**, 2811–2819 (2006).
- Davoodi, A., Pan, J., Leygraf, C., Parvizi, R. & Norgren, S. An insight into the influence of morphological and compositional heterogeneity of an individual intermetallic particle on aluminium alloy corrosion initiation. *Mater. Corros.* **64**, 195–198 (2013).
- Boag, A. et al. How complex is the microstructure of AA2024-T3? *Corros. Sci.* **51**, 1565–1568 (2009).
- Li, M., Wiame, F., Seyeux, A., Marcus, P. & Swiatowska, J. Effect of thermal oxidation on surface chemistry and elemental segregation of Al-Cu-Li alloy. *Appl. Surf. Sci.* **534**, 147633 (2020).
- Viejo, F. et al. Enhanced performance of the AA2050-T8 aluminium alloy following excimer laser surface melting and anodising processes. *Thin Solid Films* **518**, 2722–2731 (2010).
- Ma, Y. et al. Localized corrosion in AA2099-T83 aluminum-lithium alloy: the role of intermetallic particles. *Mater. Chem. Phys.* **161**, 201–210 (2015).
- MacRae, C. M. et al. An examination of the composition and microstructure of coarse intermetallic particles in AA2099-T8, including Li detection. *Microsc. Microanal.* **24**, 325–341 (2018).
- Zhu, Y., Sun, K. & Frankel, G. Intermetallic phases in aluminum alloys and their roles in localized corrosion. *J. Electrochem. Soc.* **165**, C807–C820 (2018).
- Liao, C.-M. & Wei, R. P. Galvanic coupling of model alloys to aluminum—a foundation for understanding particle-induced pitting in aluminum alloys. *Electrochim. Acta* **45**, 881–888 (1999).
- Ghosh, S. *Effect of stress on initiation and propagation of localized corrosion in aluminium alloys*, Ph.D. thesis, (University of Birmingham, 2008).
- Boettcher, T., et al. *On the intermetallic corrosion of Cu-Al wire bonds*, in 2010 12th Electronics Packaging Technology Conference, 585–590 (IEEE, 2010).
- Yasuda, M., Weinberg, F. & Tromans, D. Pitting corrosion of Al and Al-Cu single crystals. *J. Electrochem. Soc.* **137**, 3708–3715 (1990).
- Zhou, X. et al. Copper enrichment in Al-Cu alloys due to electropolishing and anodic oxidation. *Thin Solid Films* **293**, 327–332 (1997).
- Zhu, Y. & Franke, G. Effect of major intermetallic particles on localized corrosion of AA 2060-T8. *Corrosion* **75**, 29–41 (2019).

59. Lacroix, L., Ressler, L., Blanc, C. & Mankowski, G. Combination of AFM, SKPFM and SIMS to study the corrosion behavior of s-phase particles in AA2024-T351. *J. Electrochem. Soc.* **155**, C131 (2008).
60. Costa, D., Ribeiro, T., Mercuri, F., Pacchioni, G. & Marcus, P. Atomistic modeling of corrosion resistance: a first principles study of O<sub>2</sub> reduction on the al (111) surface covered with a thin hydroxylated alumina film. *Adv. Mater. Interfaces* **1**, 1300072 (2014).

## ACKNOWLEDGEMENTS

Région Île-de-France is acknowledged for partial funding of the ToF-SIMS equipment.

## AUTHOR CONTRIBUTIONS

M.L.: experimental work, data analysis and interpretation, draft writing. A.S.: ToF-SIMS measurements, analysis and paper revision. F.W. and P.M.: discussion, paper revision, data interpretation. J.Ś.: conceptualization, scientific supervision, data analysis and interpretation, paper writing and corrections.

## COMPETING INTERESTS

The authors declare no competing interests.

## ADDITIONAL INFORMATION

**Correspondence** and requests for materials should be addressed to J.Św.

**Reprints and permission information** is available at <http://www.nature.com/reprints>

**Publisher's note** Springer Nature remains neutral with regard to jurisdictional claims in published maps and institutional affiliations.



**Open Access** This article is licensed under a Creative Commons Attribution 4.0 International License, which permits use, sharing, adaptation, distribution and reproduction in any medium or format, as long as you give appropriate credit to the original author(s) and the source, provide a link to the Creative Commons license, and indicate if changes were made. The images or other third party material in this article are included in the article's Creative Commons license, unless indicated otherwise in a credit line to the material. If material is not included in the article's Creative Commons license and your intended use is not permitted by statutory regulation or exceeds the permitted use, you will need to obtain permission directly from the copyright holder. To view a copy of this license, visit <http://creativecommons.org/licenses/by/4.0/>.

© The Author(s) 2021